ELSEVIER

Journal of Alloys and Compounds 403 (2005) 245–257

Journal of ALLOYS AND COMPOUNDS

www.elsevier.com/locate/jallcom

Derivation of the liquidus surface projection for the Al–Pt–Ru system from as-cast samples

S.N. Prins [a,*], L.A. Cornish [b,c], P.S. Boucher [a]

[a] *CSIR-NML, P.O. Box 395, Pretoria 0001, South Africa*
[b] *Advanced Materials Division, Mintek, Private Bag X3015, Randburg 2125, South Africa*
[c] *DST/NRF Centre of Excellence for Strong Materials, University of the Witwatersrand, South Africa*

Received 2 April 2005; received in revised form 1 June 2005; accepted 2 June 2005
Available online 30 September 2005

Abstract

The liquidus surface projection for the Al–Pt–Ru ternary system has been determined based on the microstructural characterisation of arc-melted alloys. The liquidus surface is dominated by the ∼RuAl phase, and slopes down to the Al-rich corner. Two new ternary phases ∼$Ru_{12}Pt_{15}Al_{73}$ and ∼$Ru_{18}Pt_{28}Al_{64}$ were observed near the Al-corner. The ∼$Ru_{12}Pt_{15}Al_{73}$ phase has a primitive cubic structure, lattice parameter of ∼0.7721 nm, and is stable to room temperature. The ∼$Ru_{18}Pt_{28}Al_{64}$ phase is a high-temperature phase, and decomposes to form ∼$Ru_{12}Pt_{15}Al_{73}$ and ∼$PtAl_2$. There is a ternary eutectic near 23 at.% Al, 55 at.% Pt and 22 at.% Ru, whereas most of the other reactions were identified from their microstructures as being peritectic in nature. ∼RuAl was found to contain at least 27 at.% Pt and the ∼$PtAl_2$ phase exhibited up to 11 at.% solubility for ruthenium. ∼$RuAl_6$ showed solubility of at least 10 at.% platinum. Most of the other phases showed more limited solubilities for the ternary element: ∼$RuAl_2$, ∼Pt_2Al_3 and ∼PtAl contained only about 2 at.% of the third component. ∼Ru_4Al_{13} has less than 1 at.% solubility for platinum.

Keywords: Intermetallics; Scanning electron microscopy; X-ray diffraction

1. Introduction

In a study to develop Pt-based alloys for high-temperature applications, quaternary Pt-based alloys were manufactured and exhibited two-phase γ/γ′ structures analogous to the nickel-based superalloys [1]. The quaternary alloy Pt_{84}:Al_{11}:Ru_2:Cr_3 was identified as the best in terms of microstructure and hardness. Further to developing the alloys, a second purpose of the project is to develop a CALPHAD-type thermodynamic database so that suitable higher order alloy compositions can be derived quickly. In order to facilitate this, studies of the component ternary phase diagrams from Pt–Al–Cr–Ru had to be undertaken.

The Pt-rich corner is of importance for the Pt-based alloys for high-temperature applications. The RuAl phase from the Al–Ru binary is a very stable, high-temperature, high-strength ordered intermetallic compound which has potential in applications requiring high strength at high temperatures in environmentally harsh conditions. RuAl was also recently earmarked in another study as a possible bond-coat material [2] in Ni-based superalloy coating technology.

2. Previous work

2.1. Aluminium–platinum

The Pt–Al phase diagram is complex and although certain features have been determined reliably, the Pt-rich end especially, remains uncertain. Huch and Klemm [3] reported platinum to be practically insoluble in (Al), and observed the eutectic formation of (Al) + Pt_5Al_{21} at 627 °C. Pt_5Al_{21}

* Corresponding author. Present address: Department of Materials Science and Engineering, Pennsylvania State University, University Park, PA 16802, USA.
E-mail addresses: snp131@psu.edu, sprins@csir.co.za (S.N. Prins).

0925-8388/$ – see front matter © 2005 Published by Elsevier B.V.
doi:10.1016/j.jallcom.2005.06.004

forms by a peritectic reaction from Pt_8Al_{21} at 806 °C and has a complex cubic stoichiometric structure with very limited solubility. Huch and Klemm [3] reported cubic 'PtAl$_4$' with ~20 at.% Pt, and suggested that the phase might be Pt_5Al_{21}. Piatti and Pellegrini [4] confirmed this, and Guex and Feshotte [5] also reported a complex cubic phase: PtAl$_4$ or Pt_5Al_{21}. Schaller [6] reported hexagonal Pt_5Al_{21} phase, whereas Ellner et al. [7] designated the hexagonal phase as PtAl$_4$. Piatti and Pellegrini [4] also reported a hexagonal phase in the same region, and observed transformation to a cubic structure below 200 °C. On the basis of these observations, PtAl$_4$ has been suggested as a metastable phase in the Pt–Al system.

The stoichiometric Pt_8Al_{21} phase forming peritectically from PtAl$_2$ was confirmed by Edshammar [8] and Ellner et al. [7] after the earlier reports by Huch and Klemm [3] and Guex and Feshotte [5] of a PtAl$_3$-like phase. The structure of Pt_8Al_{21} has not been determined. Huch and Klemm [3], Guex and Feshotte [5] and Ellner et al. [7] reported the PtAl$_2$ phase, which forms peritectically from Pt_2Al_3 at 1679 °C to have cubic CaF_2 structure. Pt_2Al_3 has a structure related to, but not isotypic with, hexagonal Ni_2Al_3 and very limited solubility range [3,5,7]. PtAl is stoichiometric with a cubic FeSi structure and forms congruently at 1554 °C.

Evidence of a β phase (B2 CsCl crystal structure) existing between 1260 and 1500 °C with a solubility range from 51 to 56 at.% Pt was reported by Chattopadhyay and Schubert [9] and Bhan and Kudielka [10]. McAlister and Kahan [11] included these observations in their assessment of the Pt–Al system and proposed a peritectic reaction: L + PtAl → β, with a eutectoid decomposition to PtAl + Pt_5Al_3. The latter corresponded to a thermal arrest of Huch and Klemm [3].

Ellner et al. [7], Oya et al. [12] and Huch and Klemm [3] reported Pt_5Al_3 to have a rhombohedral Rh_5Ge_3-type structure and form by a peritectic reaction from PtAl$_3$ and have limited solubility. Pt_2Al forms peritectoidally from PtAl$_3$ and Pt_5Al_3 at ~1430 °C. Two crystal variants have been reported, with a transformation temperature of 1060 °C.

Pt_3Al forms congruently at 1556 °C, eutectically with (Pt) at 1507 °C [3,13], as well as eutectoidally at 1280 °C. A martensitic reaction has been reported for cubic $L1_2$ Pt_3Al transforming to tetragonal DO'_c Pt_3Al on cooling. The transformation temperature has a maximum at 1290 °C, and is very composition-dependent of the Al-rich side. Mishima and coworkers [14] and Oya et al. [12] reported it at about 340 °C with another transformation at 127 °C. Biggs et al. [15] confirmed both lower transformation temperatures.

2.2. Aluminium–ruthenium

The first phase diagram was determined by Obrowski [16,17]. He reported the eutectic between RuAl and (Ru) at ~70 at.% Ru and 1920 ± 20 °C, and that (Ru) dissolves up to 4 at.% Al. RuAl formed congruently at 2060 ± 20 °C and underwent a peritectic reaction at ~1600 °C and 40 at.% Ru to form Ru_2Al_3. Both RuAl and Ru_2Al_3 had wide composition ranges (up to 9 at.%) and Ru_2Al_3 decomposed eutectoidally at ~1000 °C. Other phases reported were: RuAl$_2$, RuAl$_3$, RuAl$_6$ and RuAl$_{12}$. RuAl$_6$ also formed congruently and then reacted peritectically to form RuAl$_{12}$.

Subsequently, Anlage et al. [18] reported that the Al-rich end of Obrowski's phase diagram was incorrect and investigated alloys up to 26 at.% Ru. They observed the phases (Al), RuAl$_6$ and Ru_4Al_{13} (Obrowski's RuAl$_3$). From thermal analysis, the following reactions were found: L → RuAl$_6$ + (Al) at 652 °C; L + Ru_4Al_{13} → RuAl$_6$ at 723 °C; L + RuAl$_2$ → Ru_4Al_{13} at 1403 °C. RuAl$_{12}$ was not observed. Their formation temperature of RuAl$_6$ and the related eutectic reaction temperature were similar to Obrowski's formation temperatures of RuAl$_{12}$ and its associated eutectic reaction: 723 and 652 °C [18] compared to 750 and 630 °C [16], respectively.

X-ray studies have been carried out by several workers. Schwomma et al. [19] identified RuAl$_2$ and RuAl. Edshammar [20–22] investigated Ru_4Al_{13}, RuAl, Ru_2Al_3, RuAl$_2$ and a phase only observed in arc-melted samples, RuAl$_{\sim 2.5}$. The calorimetric studies of Jung and Kleppa [23] showed that RuAl has a high heat of formation, -124.1 ± 3.3 kJ mol^{-1}.

Boniface and Cornish [24,25] confirmed the work of Anlage et al. [18] and that of Obrowski [16] above ~45 at.% Ru. In addition, they reported a cascade of peritectic reactions from the RuAl phase through Ru_2Al_3, RuAl$_2$, Ru_4Al_{13} and RuAl$_6$. The formation temperature of RuAl$_2$ was inferred to be ~1460 °C. A slow exothermic reaction was observed around 50 at.% Ru during arc-melting, in agreement with the results of Jung and Kleppa [26].

The Ru_2Al_3 phase was found to be stable down to ~976 °C, which is similar to Edshammar's heat treatment temperature [21]. Their phase diagram [24] incorporated Obrowski's data [16] above 50 at.% Ru, and data from Anlage et al. [18] up to 26 at.% Ru.

Mi et al. [27] recently proposed changes to the Al-rich equilibrium. They found the Ru_2Al_5 phase stable as a high-temperature stoichiometric phase, forming peritectically from RuAl$_2$ at 1482 °C and decomposing eutectoidally at 1340 °C to form Ru_4Al_{13} and RuAl$_2$. They suggested that RuAl$_2$ forms peritectically at 1805 °C from RuAl, while the stability at lower temperatures is uncertain. They also reported room-temperature stability for Ru_2Al_3 and did not report any solubility range.

It has been suggested by Wolff [28] that the L → RuAl + (Ru) eutectic occurs at higher Ru contents than the current diagrams, which has been confirmed by Ilić et al. [29]. Mücklich and Ilić [30] recently published a detailed review of RuAl and its alloys.

2.3. Platinum–ruthenium

In the Pt–Ru system, about 62 at.% Ru dissolves in the platinum-rich solid solution at 1000 °C [31].

A two-phase region of (Pt) and (Ru) exists between ~62 and ~80 at.% Pt. A ruthenium-rich solid solution is observed

above ∼80 at.% Ru at 1000 °C. (Pt) forms by a peritectic reaction at ∼2120 °C.

2.4. Platinum–aluminium–ruthenium

The only work published on the Pt–Al–Ru system outside this study is by Biggs [32] and Biggs et al. [15], and this was for high Pt content alloys. A partial isothermal section at 1350 °C showed that (Ru) was in equilibrium with $L1_2$ $\sim Pt_3Al$, and (Pt) was in equilibrium with the tetragonal form of $\sim Pt_3Al$.

3. Experimental procedure

Sixteen samples were prepared by arc-melting, using elemental powders of at least 99.9 percent purity. The mass losses of the samples were monitored; only one sample had a mass loss greater than 5%. The samples were cut in two, mounted in a conductive resin and prepared metallographically to a 0.25 μm finish for characterisation.

The microstructures were studied using light microscopy, and secondary electron and backscattered electron imaging in a LEO 1525 FE-SEM scanning electron microscope (SEM). Energy dispersive X-ray spectroscopy (EDS) in the SEM was used to determine overall and phase compositions using an Oxford INCA EDS detector and pure elemental standards.

The phases were identified by their compositions, formation order and morphology with SEM/EDS. X-ray diffraction (XRD) was used to verify the phase identification, identify crystal structures and calculate the lattice parameters. The XRD was undertaken using a Philips X-ray diffractometer with monochromated Cu Kα radiation, using a continuous scan from 4 to 90° 2θ with step size of 0.02° and dwell time of 0.5 s. Spectra were matched with standard spectra from the ICDD [33] and ISCD databases [34] for the expected phases. Prototypes and modelled diffraction patterns were used where no standard was available. The diffraction patterns were modelled using the Crystallographica© software [35]. Since the presence of a third element in the binary phases shifted the diffraction patterns of the phases significantly, the lattice parameters were refined using the WinCell© software [36].

Differential thermal analysis was undertaken on selected samples using a Seteram TGDTA 92 under an argon atmosphere and with alumina crucibles. The scan rate was 10 °C min^{-1}. Each sample was scanned twice, and the data were recorded on heating.

4. Results

The EDS overall and phase analyses are given in Table 1, and each specimen is described individually. Although some aluminium was lost on manufacture, the actual compositions were near those targeted.

4.1. $\sim Al_{21}:Pt_{51}:Ru_{28}$ (Alloy 6)

On sample preparation, the nominal $\sim Al_{21}:Pt_{51}:Ru_{28}$ alloy showed ductility. The primary phase was coarse (Ru) needles, and these were surrounded by a binary eutectic comprising (Ru) and $\sim Pt_3Al$ with, further away from the needles, a ternary eutectic comprising (Ru), $\sim Pt_3Al$ and very fine dendritic-like particles of (Pt) (Fig. 1). The solidification sequence was deduced to be: (Ru) needles formed initially, then a eutectic of (Ru) and $\sim Pt_3Al$, and finally, the ternary eutectic: (Ru) + ∼ Pt_3Al + (Pt). The EDS analyses are shown in Table 1, although the (Pt) phase in the ternary eutectic is not indicated, as the phase was too small to analyse quantitatively. However, the very fine needles did show a higher Pt content. The ternary eutectic had a composition of 22.9 ± 1.0 at.% Al, 55.4 ± 1.5 at.% Pt and 21.7 ± 2.2 at.% Ru.

4.2. $\sim Al_{30}:Pt_{54}:Ru_{16}$ (Alloy 12)

The nominal $\sim Al_{30}:Pt_{54}:Ru_{16}$ alloy comprised fine (Ru) needles in a Pt_5Al_3 matrix. The needles were finer than the primary (Ru) needles observed in the as-cast ∼ $Al_{21}:Pt_{51}:Ru_{28}$ alloy, and there was no evidence of the ternary eutectic. The alloy showed similar ductility to the $\sim Al_{21}:Pt_{51}:Ru_{28}$ alloy.

4.3. $\sim Al_{42}:Pt_{56}:Ru_2$ (Alloy 15)

The $Al_{42}:Pt_{56}:Ru_2$ alloy did not show any brittleness. At low magnification, the BSE images showed areas of different morphology; at higher magnifications, a two-phase structure was observed in the matrix with two different finenesses: coarse and fine (Fig. 2). On solidification, β phase formed initially, followed by a eutectic reaction forming β and Pt_5Al_3,

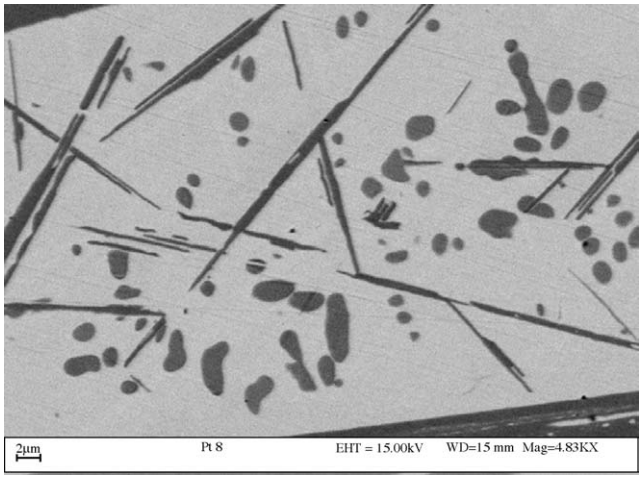

Fig. 1. SEM image in backscattered electron mode of $\sim Al_{21}:Pt_{51}:Ru_{28}$ (Alloy 6) showing: primary (Ru) needles (dark) partially seen at the top and bottom, with smaller (Ru) needles in a $\sim Pt_3Al$ matrix (light) and (Pt) rounded particles (medium dark).

Table 1
EDS analyses of the alloys and their phases

Alloy number	Composition (at.%)														
	Overall	(Pt)	(Ru)	~Pt_3Al	Pt_5Al_3	~PtAl	~RuAl	Pt_2Al_3	~$RuAl_2$	~$PtAl_2$	~$Ru_{12}Pt_{15}Al_{73}$	~Ru_4Al_{13}	~Pt_8Al_{21}	(Al)	$RuAl_6$
6															
Al	21.4 ± 0.7	29.0 ± 1.2	1.8 ± 0.6	28.6 ± 0.8											
Pt	51.7 ± 0.5	68.7 ± 1.7	17.8 ± 1.1	69.5 ± 0.8											
Ru	26.2 ± 0.9	2.3 ± 1.1	80.4 ± 1.6	1.9 ± 0.5											
12															
Al	29.9 ± 0.6		0		34.9 ± 0.4										
Pt	54.3 ± 0.7		10.2 ± 2.3		65.1 ± 0.4										
Ru	15.8 ± 0.6		89.8 ± 2.3		0										
15															
Al	42.0 ± 0.3				35.0 ± 0.4	45.2 ± 0.2									
Pt	55.7 ± 0.8				61.9 ± 0.6	52.1 ± 0.7									
Ru	2.3 ± 0.7				3.1 ± 0.5	2.7 ± 0.6									
10															
Al	28.0 ± 0.6		3.3 ± 0.3		40.5 ± 3.6		42.3 ± 0.7								
Pt	32.6 ± 0.5		3.4 ± 0.3		59.5 ± 3.6		21.3 ± 0.6								
Ru	39.5 ± 1		93.3 ± 0.5		0		36.4 ± 0.8								
11															
Al	39.7 ± 0.8				37.6 ± 0.4	42.9 ± 0.9	42.4 ± 0.7								
Pt	50.1 ± 0.9				62.4 ± 0.4	44.4 ± 3.3	23.5 ± 0.8								
Ru	10.2 ± 1.1				0	12.7 ± 2.8	34.1 ± 0.9								
4															
Al	51.6 ± 0.5					47.4 ± 2	45.3 ± 1.2	55.2 ± 0.6							
Pt	40.9 ± 3					52.6 ± 2	27.3 ± 1.4	44.8 ± 0.6							
Ru	7.6 ± 3.2					0	27.4 ± 1.6	0							
5															
Al	43.6 ± 0.9					41.1 ± 1	45.3 ± 0.6								
Pt	26.5 ± 0.8					52.9 ± 2.5	17.1 ± 0.6								
Ru	29.9 ± 1.3					6.0 ± 2.3	37.6 ± 0.8								
9															
Al	55.7 ± 0.8						47.6 ± 0.7	59.6 ± 0.5							
Pt	32.9 ± 0.9						20.6 ± 0.3	40.4 ± 0.5							
Ru	11.4 ± 1.4						31.5 ± 1.9	0							
3															
Al	54.3 ± 0.8						49.4 ± 3		63.2 ± 1.1	57.3 ± 1.3	69.6 ± 1.1				
Pt	13.8 ± 0.9						12.3 ± 1		1.3 ± 0.5	31.1 ± 1	14.0 ± 1.4				
Ru	31.9 ± 0.9						38.3 ± 3.2		35.5 ± 1.8	11.6 ± 1.9	16.4 ± 1.9				
8															
Al	62.0 ± 0.5						56.2 ± 0.8		67.0 ± .6	61.7 ± 1					
Pt	6.2 ± 0.4						2.6 ± 0.8		10.4 ± 0.3	30.4 ± .2					
Ru	31.8 ± 0.7						41.2 ± 0.8		22.6 ± 0.7	7.9 ± .1					

14								
	Al	64.0 ± 0.4	63.9 ± 0.5	57.8 ± 0.6	69.7 ± 0.5			
	Pt	13.6 ± 0.4	~0	32.4 ± 1.1	13.9 ± 0.7			
	Ru	22.4 ± 0.2	36.1 ± 0.5	9.8 ± 0.9	16.4 ± 1.0			
16								
	Al	71.8 ± 0.4	63.7 ± 0.3	65.4 ± 0.9	71.8 ± 1.6	74.3 ± .2		
	Pt	9 ± 0.3	0.5 ± 0.2	34.6 ± 0.9	19.1 ± 1.3	0.5 ± .2		
	Ru	19.2 ± 0.3	35.8 ± 0.3	~0	9.1 ± 2.5	25.2 ± .2		
2								
	Al	65.5 ± 0.5		61.5 ± 0.3	70.5 ± 0.4			
	Pt	26.9 ± 0.4		32.6 ± 0.3	16.6 ± 0.2			
	Ru	7.6 ± 0.4		5.9 ± 0.5	12.9 ± 0.4			
7								
	Al	70.8 ± 0.4		67.9 ± 1	72.1 ± 1.2			
	Pt	21.6 ± 0.4		32.1 ± 1	18.4 ± 1.2			
	Ru	7.6 ± 0.6		0	9.5 ± 2.2			
13								
	Al	87.6 ± 0.4			73.4 ± 0.4		76.8 ± 0.7	100
	Pt	8.5 ± 0.4			17.1 ± 0.8		24.2 ± 0.8	0
	Ru	4.0 ± 0.4			9.5 ± 0.7		0	0
1								
	Al	84.0 ± 0.6			76.1 ± 1		75.1 ± 0.2	100
	Pt	8.5 ± 0.5			10.5 ± 0.7		20.8 ± 0.5	0
	Ru	7.5 ± 0.6			13.4 ± 0.6		4.1 ± 0.5	0

Fig. 2. SEM image in backscattered mode of ~Al_{42}:Pt_{56}:Ru_2 (Alloy 15) showing the varying morphology for eutectic (coarser) and prior dendritic (finer) regions: ~Pt_5Al_3 (light) and ~PtAl (dark).

which was the coarser structure. The β phase subsequently decomposed in the solid-state to form ~PtAl and ~Pt_5Al_3, which comprised the finer structure.

4.4. ~Al_{28}:Pt_{33}:Ru_{39} (Alloy 10)

The as-cast microstructure showed (Ru) dendrites sometimes within dendrites of ~RuAl, and often surrounded by a fine two-phase structure, with the matrix Pt_5Al_3 (Fig. 3). There were two peritectic reactions: forming ~RuAl from (Ru), and then β forming from ~RuAl. The β subsequently decomposed in the solid-state to form the fine two-phase structure of ~PtAl and Pt_5Al_3, and Pt_5Al_3 precipitated in ~RuAl, showing that the ~RuAl solvus slopes with decreasing temperature.

Fig. 3. SEM image in backscattered electron mode of ~Al_{28}:Pt_{33}:Ru_{39} (Alloy 10) showing (Ru) dendrites (dark) surrounded by ~RuAl (medium) and Pt_5Al_3 (light).

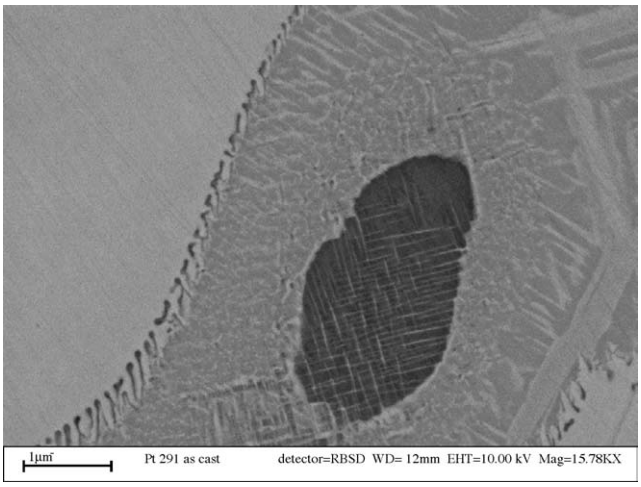

Fig. 4. SEM image in backscattered electron mode of ∼Al_{40}:Pt_{50}:Ru_{10} (Alloy 11) showing ∼RuAl (dark), ∼PtAl (medium) and Pt_5Al_3 (light).

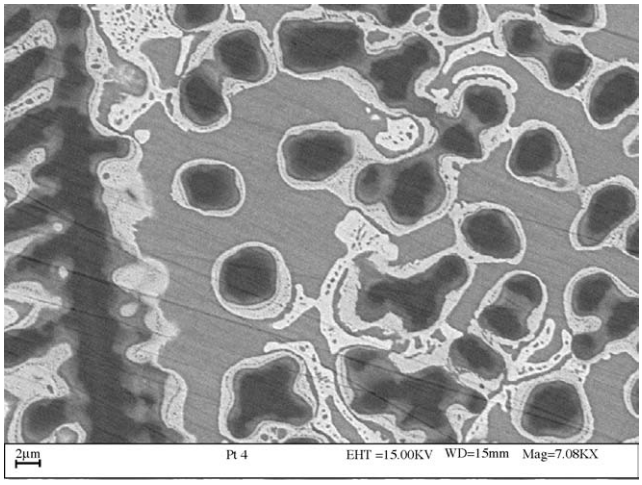

Fig. 5. SEM image in backscattered electron mode of ∼Al_{52}:Pt_{40}:Ru_8 (Alloy 4) showing ∼RuAl (dark), PtAl (light) and Pt_2Al_3 (medium).

4.5. ∼Al_{40}:Pt_{50}:Ru_{10} (Alloy 11)

At low magnification, the microstructure showed dark ∼RuAl dendrites surrounded by a medium contrast ∼PtAl phase in a lighter Pt_5Al_3 matrix. However, at higher magnification, both the medium and darker regions were actually two-phase, and there were laths suggesting a solid-state transformation to form the light phase within the medium phase (Fig. 4). After solidification, there was also precipitation of fine light needles in the primary dark phase. By extrapolation (since two of the phases were too fine to analyse accurately), and using the XRD results together with data from nearby alloys, the medium contrast phase was deduced to be ∼PtAl. There were two peritectic reactions, forming β from ∼RuAl, then subsequently forming Pt_5Al_3 from β. After solidification, the β phase decomposed to form Pt_5Al_3 + ∼PtAl (giving the two-phase microstructure), and there was precipitation of a lighter phase (Pt_5Al_3) in ∼RuAl and ∼PtAl.

4.6. ∼Al_{52}:Pt_{40}:Ru_8 (Alloy 4)

The Al_{52}:Pt_{40}:Ru_8 alloy was brittle. The microstructure showed cored and irregular ∼RuAl dendrites surrounded by an irregular eutectic comprising PtAl + Pt_2Al_3 (Fig. 5). The uneven outline of the irregular ∼RuAl dendrites showed that a peritectic reaction had occurred, and the formation of the eutectic indicated that the liquid composition had passed through, or very near to, the invariant reaction: L + ∼RuAl → PtAl + Pt_2Al_3. The overall analysis of the eutectic was 45.8±1.0 at.% Al, 43.0±1.0 at.% Pt and 11.2 ± 1.0 at.% Ru. The last phase to form was Pt_2Al_3.

4.7. ∼Al_{44}:Pt_{26}:Ru_{30} (Alloy 5)

The Al_{44}:Pt_{26}:Ru_{30} alloy was extremely brittle. The microstructure comprised cored ∼RuAl dendrites with a two-phase interdendritic infill (Fig. 6). Peritectic formation of β from ∼RuAl was deduced from the irregular outline of the ∼RuAl. The β phase decomposed in the solid-state, as in the binary Al–Pt phase diagram [31], to form ∼PtAl + Pt_5Al_3. The overall analyses of the two-phase ∼PtAl + Pt_5Al_3 areas were 44.6±0.5 at.% Al, 48.4 ± 0.5 at.% Pt and 7.0±0.2 at.% Ru, which is an indication of the composition of the β phase prior to its decomposition.

4.8. ∼Al_{55}:Pt_{33}:Ru_{11} (Alloy 9)

The Al_{55}:Pt_{33}:Ru_{11} alloy exhibited only two phases and it was rather difficult to distinguish between them using backscattered electron imaging. However, the compositions were quite different (Table 1), and so the contrast was unlikely to be caused by coring. The dendrites were ∼RuAl and the matrix was Pt_2Al_3.

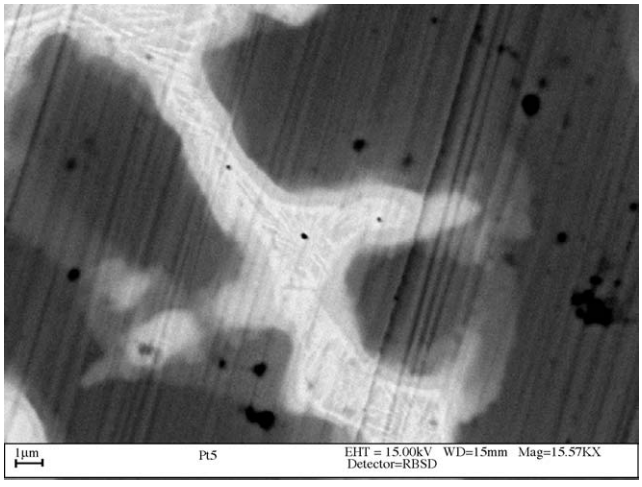

Fig. 6. SEM image in backscattered electron mode of ∼Al_{44}:Pt_{26}:Ru_{30} (Alloy 5) showing dark ∼RuAl dendrites with light ∼PtAl and very light Pt_5Al_3.

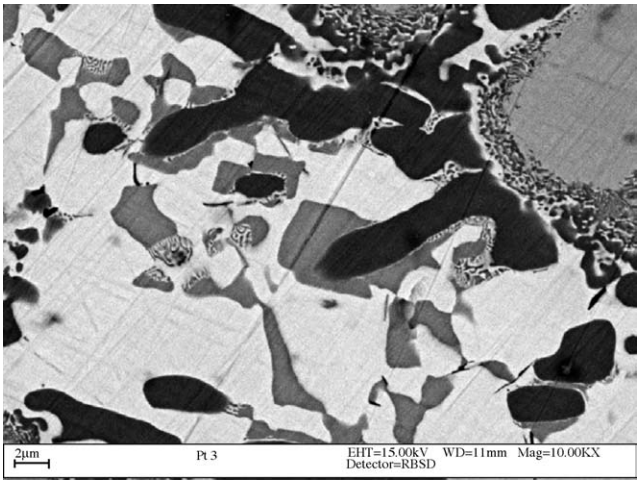

Fig. 7. SEM image in backscattered electron mode of ~Al_{54}:Pt_{14}:Ru_{32} (Alloy 3) showing ~RuAl (dendritic regions of medium grey), decomposed ~Ru_2Al_3 (larger two-phase regions of ~RuAl + ~$RuAl_2$), ~$RuAl_2$ (dark), $PtAl_2$ (light) and ~$Ru_{12}Pt_{15}Al_{73}$ (blocky regions of dark grey), with decomposed ~$Ru_{18}Pt_{28}Al_{64}$ (smaller two-phase regions).

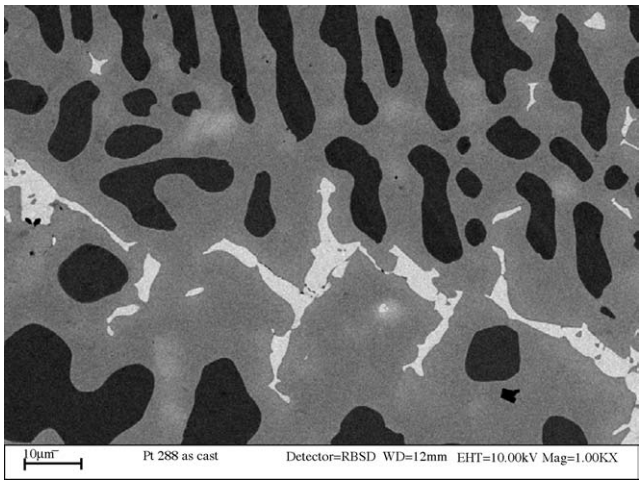

Fig. 8. SEM image in backscattered electron mode of ~Al_{62}:Pt_6:Ru_{32} (Alloy 8) showing ~RuAl (dark), ~$RuAl_2$ (medium contrast) and lastly very irregular patches of ~$PtAl_2$ (light).

4.9. ~Al_{54}:Pt_{14}:Ru_{32} (Alloy 3)

Four phases were observed in the Al_{57}:Pt_{12}:Ru_{31} specimen (Fig. 7). Dendrites of ~RuAl solidified first, and there was a two-phase mixture surrounding them. Since the two phases were ~RuAl and ~$RuAl_2$, the products of the eutectoid decomposition of Ru_2Al_3 [31], it was deduced that Ru_2Al_3 formed peritectially from ~RuAl, just as in the Al–Ru binary. Chunky $RuAl_2$ solidified on the (subsequently decomposed) Ru_2Al_3. The solidification then proceeded in one of two ways locally (depending on local composition): either the ~$RuAl_2$ through a series of peritectic reactions so that the final product was ~$PtAl_2$, or the ~$RuAl_2$ reacted with the liquid to form a ternary phase ~$Ru_{18}Pt_{28}Al_{64}$, which then formed ~$Ru_{12}Pt_{15}Al_{73}$, another ternary phase, in a peritectic reaction. The ~$Ru_{18}Pt_{28}Al_{64}$ ternary phase also decomposed at lower temperatures, which explains the fine structures between $RuAl_2$ and the ternary phase ~$Ru_{12}Pt_{15}Al_{73}$. The overall analysis of the fine ~$Ru_{12}Pt_{15}Al_{73}$ + ~$PtAl_2$ areas which had been ~$Ru_{18}Pt_{28}Al_{64}$ were too small to analyse accurately in these alloys without collecting signals from the surrounding phases.

4.10. ~Al_{62}:Pt_6:Ru_{32} (Alloy 8)

The ~Al_{62}:Pt_6:Ru_{32} alloy was brittle, and exhibited ~RuAl dendrites surrounded by ~$RuAl_2$, and lastly, very irregular patches of ~$PtAl_2$ (Fig. 8). A cascade of peritectic reactions was deduced to form this sequence. The ~$RuAl_2$ showed some coring.

4.11. ~Al_{64}:Pt_{14}:Ru_{22} (Alloy 14)

Nominal ~Al_{64}:Pt_{14}:Ru_{22} was brittle and fractured easily. There were three distinct phases: dendritic ~$RuAl_2$, surrounded by peritectically formed ~$Ru_{12}Pt_{15}Al_{73}$, and the remaining phase, ~$PtAl_2$, which also formed via a peritectic reaction (Fig. 9).

The thermograms showed much noise, but two peaks could be discerned by their size, shape and reproducibility. These were at $1511.7 \pm 5\,^{\circ}C$ (onset, peaking at $1520.2 \pm 5\,^{\circ}C$) identified for ~$Ru_{12}Pt_{15}Al_{73}$ solidification, and $1373.4 \pm 5\,^{\circ}C$ (onset, peaking at $1384.2 \pm 5\,^{\circ}C$) for ~$PtAl_2$.

4.12. ~Al_{72}:Pt_9:Ru_{19} (Alloy 16)

The ~Al_{72}:Pt_9:Ru_{19} sample was the product of primary solidification of ~$RuAl_2$ followed by a cascade of peritectic reactions, forming in turn: ~Ru_4Al_{13}, ~$Ru_{12}Pt_{15}Al_{73}$ and ~$PtAl_2$ (Fig. 10).

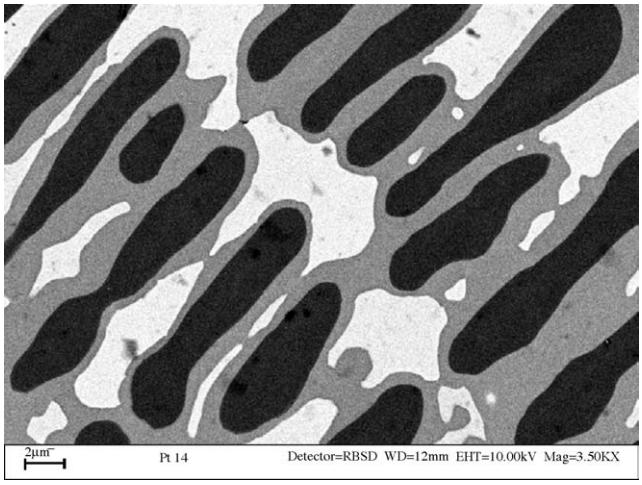

Fig. 9. SEM image in backscattered electron mode of ~Al_{64}:Pt_{14}:Ru_{22} (Alloy 14) showing $RuAl_2$ dendrites (dark), ~$Ru_{12}Pt_{15}Al_{73}$ (medium) and ~$PtAl_2$ (light).

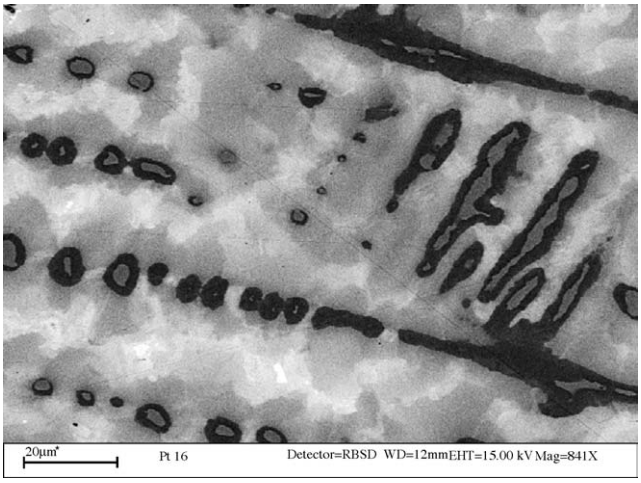

Fig. 10. SEM image in backscattered of $\sim Al_{72}:Pt_9:Ru_{19}$ (Alloy 16) showing: $\sim RuAl_2$ (dark) surrounded by very dark $\sim Ru_4Al_{13}$, cored $\sim Ru_{12}Pt_{15}Al_{73}$ (medium to light), with tiny amount of $PtAl_2$ (very light).

4.13. $\sim Al_{65}:Pt_{27}:Ru_8$ (Alloy 2)

The primary phase was identified as $\sim Ru_{18}Pt_{28}Al_{64}$ on the basis of the morphology and composition. After being mainly consumed in a peritectic reaction to form $\sim PtAl_2$, the remaining $\sim Ru_{18}Pt_{28}Al_{64}$ subsequently decomposed eutectoidally to give $\sim Ru_{12}Pt_{15}Al_{73} + \sim PtAl_2$ (Fig. 11). The overall analysis of the decomposed inner dendrite, which should be the composition of $\sim Ru_{18}Pt_{28}Al_{64}$, was 64.0 ± 0.3 at.% Al; 28.2 ± 0.2 at.% Pt; 17.8 ± 0.3 at.% Ru. The last solidification reaction was the formation of a eutectic between $\sim PtAl_2$ and $\sim Ru_{12}Pt_{15}Al_{73}$. There was also some solid-state precipitation within $\sim PtAl_2$, demonstrating a sloping solvus.

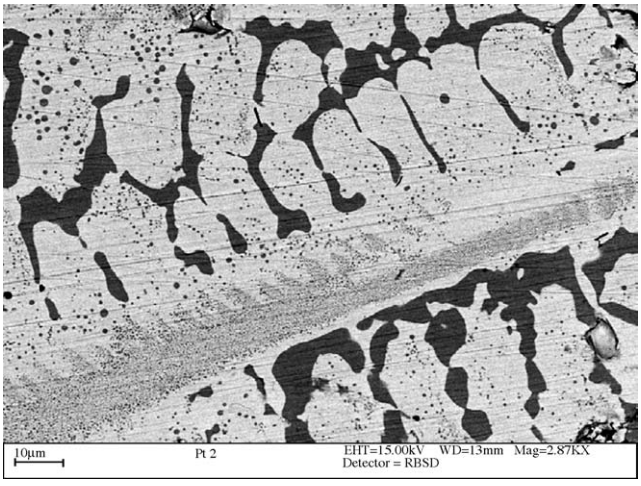

Fig. 11. SEM image in backscattered electron mode of $\sim Al_{65}:Pt_{27}:Ru_8$ (Alloy 2) showing small dendrites of $\sim Ru_{18}Pt_{28}Al_{64}$ (now decomposed to $\sim Ru_{12}Pt_{15}Al_{73}$ (dark) + $\sim PtAl_2$ (light) in a sparse eutectic of $\sim PtAl_2 + \sim Ru_{12}Pt_{15}Al_{73}$.

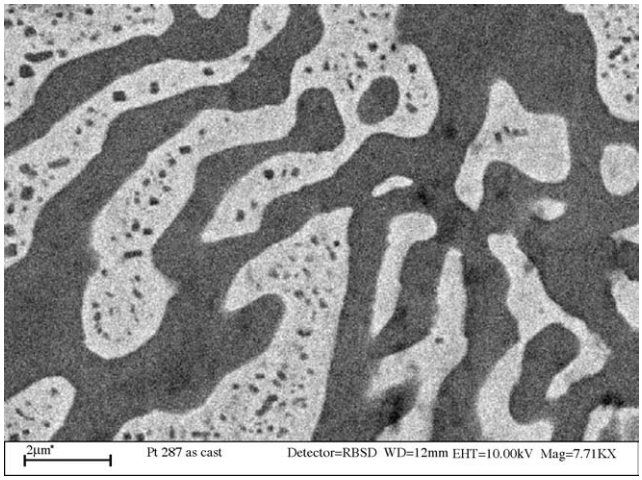

Fig. 12. SEM image in backscattered electron mode of $\sim Al_{71}:Pt_{22}:Ru_7$ (Alloy 7) showing precipitates of $\sim Ru_{12}Pt_{15}Al_{73}$ (dark) in the $PtAl_2$ dendrites (light) (the precipitate-free regions are part of the $PtAl_2 + \sim Ru_{12}Pt_{15}Al_{73}$ eutectic).

4.14. $\sim Al_{71}:Pt_{22}:Ru_7$ (Alloy 7)

Nominal $\sim Al_{71}:Pt_{22}:Ru_7$ was two-phase, consisting of $PtAl_2$ dendrites surrounded by a eutectic comprising $PtAl_2$ and $\sim Ru_{12}Pt_{15}Al_{73}$. The larger primary areas (Fig. 12) had small particles within; which suggests that the $PtAl_2$ boundary is sloping. The overall analysis of the primary areas with precipitation, which is the original primary phase composition is 64.0 ± 0.5 at.% Al, 1.0 ± 0.2 at.% Pt and 35.0 ± 0.4 at.% Ru.

There were two peaks from the DTA analyses. These were at $1299.8 \pm 5\,^{\circ}C$ (onset, peaking at $1317.1 \pm 5\,^{\circ}C$) for primary $PtAl_2$, and $1243.9 \pm 5\,^{\circ}C$ (onset, peaking at $1253.7 \pm 5\,^{\circ}C$) for the $PtAl_2 + \sim Ru_{12}Pt_{15}Al_{73}$ eutectic.

4.15. $\sim Al_{88}:Pt_8:Ru_4$ (Alloy 13)

Nominal $\sim Al_{88}:Pt_8:Ru_4$ was brittle and cracked easily. The microstructure comprised primary $\sim Ru_{12}Pt_{15}Al_{72}$ needles in a dark (Al) matrix (Fig. 13a), with fine Pt_5Al_{21} on the needles' edges. The latter phase formed peritectically, and is not discernable in the micrographs because the grey levels and gain were optimised to show the other phases. The solidification differed depending on the local composition. Hence, between the dendrites, eutectics of two different morphologies were observed: Pt_5Al_{21} + (Al) in Fig. 13a and $RuAl_6$ + (Al) in Fig. 13b. The two different eutectics were deduced by their different morphologies, surrounding phases and overall compositions, since they occurred in too small regions to be analysed accurately. Although the analyses of the Pt_5Al_{21} phase were between Pt_8Al_{21} and Pt_5Al_{21}, it was deduced to be the latter because it was a very fine phase and the analysis would therefore have been closer to the underlying $\sim Ru_{12}Pt_{15}Al_{73}$ and (Al) phases.

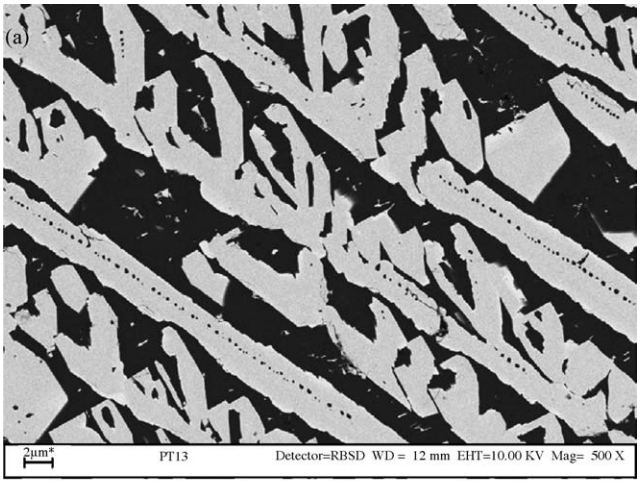

Fig. 13. SEM images in backscattered electron mode of $\sim Al_{88}$:Pt_8:Ru_4 (Alloy 13) showing the general microstructure and different morphologies of the $\sim RuAl_6$ + (Al) and Pt_5Al_{21} + (Al) eutectics: (a) large $\sim Ru_{12}Pt_{15}Al_{73}$ needles (light) with a thin layer on the edge of the needles of Pt_5Al_{21} (very light) and Pt_5Al_{21} + (Al) eutectic; (b) large $\sim Ru_{12}Pt_{15}Al_{73}$ needles (light) with a thick layer on the edge of the needles of Pt_5Al_{21} (very light) and different morphology of the $\sim RuAl_6$ + (Al) eutectic.

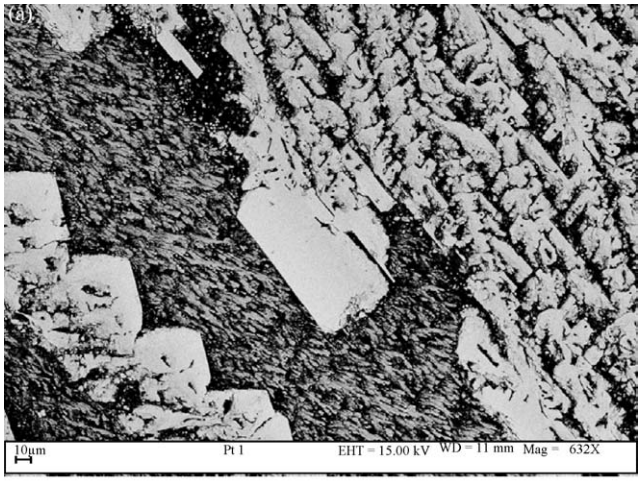

Fig. 14. SEM images in backscattered electron mode of $\sim Al_{84}$:Pt_8:Ru_8 (Alloy 1): (a) showing the two distinct microstructural areas: chunky $\sim Ru_{12}Pt_{15}Al_{73}$ (light); (b) showing detail of the finer microstructure: Pt_5Al_{21} (light) surrounded by $\sim Ru_{12}Pt_{15}Al_7$ (medium grey), $\sim RuAl_6$ (dark grey) and (Al) (black).

The DTA thermogram was difficult to interpret because of the high noise level. The only reaction that could reliably be identified was the last eutectic, forming $\sim RuAl_6$ + (Al) at 658.2 ± 5 °C (onset, peak at 699.1 ± 5 °C).

4.16. $\sim Al_{84}$:Pt_8:Ru_8 (Alloy 1)

The Al_{84}:Pt_8:Ru_8 sample exhibited two distinct different types of microstructure locally (Fig. 14), although the composition of the two phases was not significantly different ($\sim$84.3 ± 0.6 at.% Al, 8.5 ± 0.5 at.% Pt and 7.5 ± 0.6 at.% Ru for the fine region; 83.3 ± 0.6 at.% Al, 8.9 ± 0.6 at.% Pt and 7.8 ± 0.6 at.% Ru for the coarse region). The needles in the coarse region were $\sim Ru_{12}Pt_{15}Al_{73}$, which then formed $\sim RuAl_6$ peritectically, and were surrounded by a eutectic comprising $RuAl_6$ and (Al). The fine region exhibited primary solidification of Pt_5Al_{21}, followed by a cascade of peritectic reactions forming $\sim Ru_{12}Pt_{15}Al_{73}$, then $\sim RuAl_6$, and apparently finally (Al). The $\sim Ru_{12}Pt_{15}Al_{73}$ and $\sim RuAl_6$ phases were difficult to analyse since they were found together on a fine scale (Fig. 14), but they both showed solubility of at least 10 at.% platinum, although these analyses were undoubtedly influenced by the surrounding matrix. The solubility limits of platinum and ruthenium in (Al) were too low to detect. There was a difference in composition between the primary and peritectically formed $\sim Ru_{12}Pt_{15}Al_{73}$; within 1 at.% for Al, 3.5 at.% for Pt and Ru, but these were nearly within error and the already-reported range.

5. Discussion

Originally, 12 alloys were manufactured and studied, and extra alloys were made to clarify the $\sim Ru_{12}Pt_{15}Al_{73}$ phase

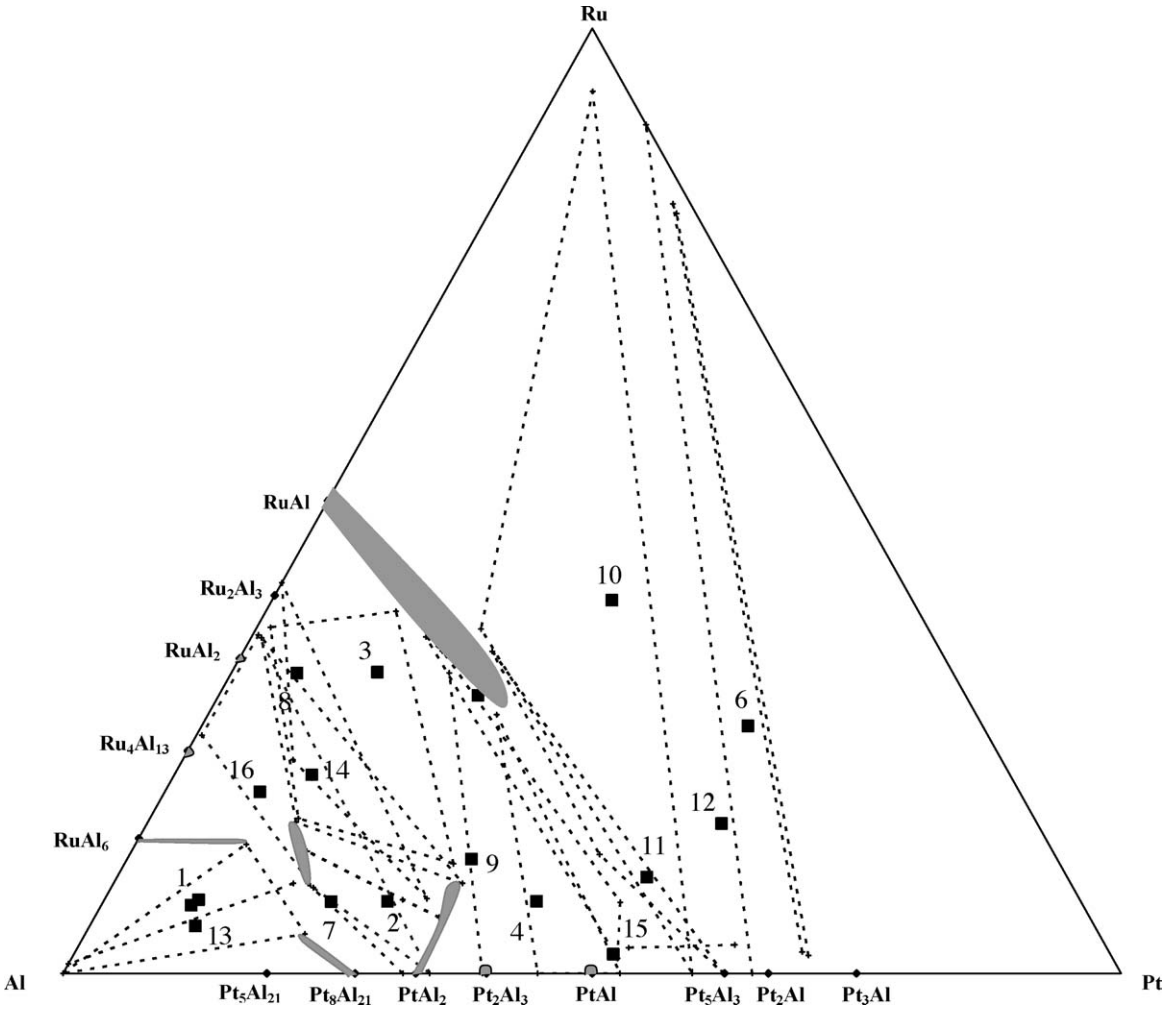

Fig. 15. Solidification projection for Al–Pt–Ru.

and the presence of the β phase from the Al–Pt phase diagram. The results from all the alloys in the as-cast state were plotted on a solidus projection (Fig. 15). This enabled some of the phases to be distinguished, and showed good agreement with the binary phase diagrams. Additionally, the phases were confirmed by X-ray diffraction. In general, there was good agreement between the experimental EDS and XRD results, despite the lack of data due to the absence of most phases in the ICDD [33]. In these cases, structure prototypes could be used with a lattice parameter refinement technique [36] to identify the binary phases and calculate lattice parameters.

X-ray diffraction also enabled the ternary phase $\sim Ru_{12}Pt_{15}Al_{73}$ to be distinguished from $\sim Ru_4Al_{13}$ [37]. The presence of the $\sim Ru_{12}Pt_{15}Al_{73}$, originally thought to be $\sim Ru_{13}Al_4$, was determined by X-ray studies of samples $\sim Al_{66}$:Pt_{26}:Ru_6 (Alloy 2), $\sim Al_{66}$:Pt_{13}:Ru_{21} (Alloy 8) and $\sim Al_{71}$:Pt_7:Ru_{22} (Alloy 14). The Al_{72}:Pt_9:Ru_{19} sample (Alloy 16) was then manufactured to ascertain that this phase, designated as $\sim Ru_{12}Pt_{15}Al_{73}$, and $\sim Ru_4Al_{13}$ were indeed different phases. The targeted composition was between the binary Ru_4Al_{13} and the least Pt-rich $\sim Ru_{12}Pt_{15}Al_{73}$ composition. Since Alloy 16 was two-phase, it proved that $\sim Ru_{12}Pt_{15}Al_{73}$ was a separate phase, and not an extension of $\sim Ru_4Al_{13}$.

Furthermore, based on the solidification sequence of the Al_{57}:Pt_{12}:Ru_{31} sample (Alloy 7), and to be consistent with the solidification projection and derived liquidus surface, it was confirmed as a ternary phase. The $\sim Ru_{12}Pt_{15}Al_{73}$ phase is isostructural to $\sim RhAl_{2.63}$ and $\sim RhAl_{2.75}$ and has a cubic structure with a lattice parameter of $\sim 0.7721 \pm 0.0005$ nm [37].

X-ray diffraction confirmed the presence of the $\sim$PtAl and $\sim Pt_5Al_3$ phases in Alloys 5, 11 and 15. The presence of these two phases confirms the existence of the β phase in the Al–Pt system because they are the eutectoid decomposition products, and the microstructure of Alloy 15 comprised both eutectic and eutectoid products, thus indicating the presence of a prior phase. However, due to the high eutectoid temperature and fast reaction kinetics, the reaction proceeded to completion, rather than leaving some β being quenched-in or retained in the structure, and the crystal structure of

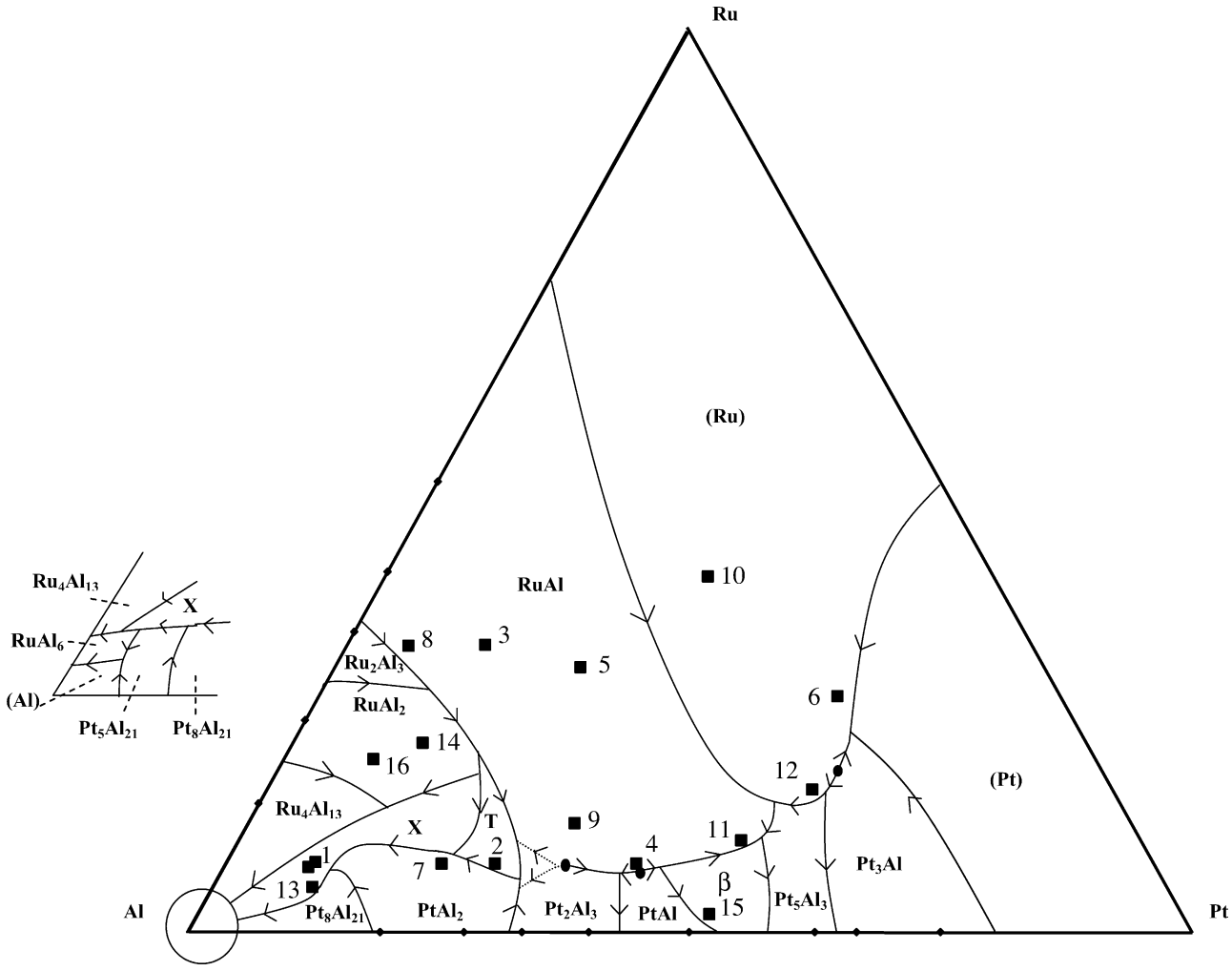

Fig. 16. Liquidus surface projection for Al–Pt–Ru. The solid squares indicate the overall compositions of the samples (are primary phase of each alloy). The ternary phases $\sim Ru_{12}Pt_{15}Al_{73}$ and $\sim Ru_{18}Pt_{28}Al_{64}$ phases are labelled X and T, respectively.

the β phase could not be confirmed in the as-cast samples. Alloys 5, 11 and 15 illustrated that the β phase formed from a liquid-reaction and then decomposed eutectoidally on cooling. Alloy 11 showed a similar $\sim Pt_5Al_3 + \sim PtAl$ eutectoid microstructure to alloy 10. Alloy 5 was mostly ∼RuAl, although the interdendritic regions comprised two distinct phases. They were too fine for accurate analysis with EDS, but the overall composition is on the tie-line connecting the two phases, indicating $\sim Pt_5Al_3$ with traces of ∼PtAl.

Alloy 3 exhibited two different regions of complex fine structures between the major phases, indicating solid-state decompositions to form those fine two-phase areas. The first comprised ∼RuAl and $\sim RuAl_2$ which is consistent with the decomposition of Ru_2Al_3 from the Al–Ru phase diagrams of Obrowski [16] and Boniface and Cornish [24,25], although not with Mi et al. [27]. The second regions were located either between $\sim RuAl_2$ and $\sim Ru_{12}Pt_{15}Al_{73}$, or between $\sim Ru_{12}Pt_{15}Al_{73}$ and $\sim PtAl_2$. If the latter case, they invariably were contained within the likely original boundary of the $\sim Ru_{12}Pt_{15}Al_{73}$ phase, suggesting that the latter formed from the parent phase in a "weak" peritectic reaction: $L + \sim Ru_{18}Pt_{28}Al_{64} \rightarrow \sim Ru_{12}Pt_{15}Al_{73} + \sim PtAl_2$. These two-phase regions contained $\sim PtAl_2$ and $\sim Ru_{12}Pt_{15}Al_{73}$. Thus, the parent phase is deduced to form peritectically from $\sim RuAl_2$, and to decompose eutectoidally into $\sim PtAl_2$ and $\sim Ru_{12}Pt_{15}Al_{73}$. The overall composition of the resulting eutectoid two-phase area was taken as the composition of the parent phase, which was close to $\sim Ru_{18}Pt_{28}Al_{64}$. Primary $\sim Ru_{18}Pt_{28}Al_{64}$ formed in Alloy 2 (Fig. 11) and subsequently decomposed, to give two-phase $\sim Ru_{12}Pt_{15}Al_{73}$ and $\sim PtAl_2$, leaving remnants of the dendrites within the light $\sim PtAl_2$ dendrites.

The interpretation of the measured reaction temperatures (from DTA) for Alloy 7 is consistent with the high formation temperature of $RuAl_2$ of Boniface and Cornish [24], because this phase would have solidified beyond the temperature capability of the DTA used. The interpreta-

tion is also consistent with the binary reaction temperatures of the binary systems. For Alloy 13, the temperature of 658.2 ± 5 °C (onset, peak at 699.1 ± 5 °C) for the ∼$RuAl_6$ + (Al) eutectic is consistent with Anlage et al.'s value of 652 °C [18]. The current value is higher than the binary value [18], which is expected because the measured reaction is within the ternary and is running down to the Al–Ru binary. The peak (actually an endothermic trough) was also consistent of a locus of a binary eutectic reaction in a ternary system because it was wider and shallower than for solidification of a single phase with little composition variation.

The microstructures have shown that there is a ternary eutectic near 23 at.% Al, 55 at.% Pt and 22 at.% Ru (Fig. 1). Most of the other reactions were identified from their microstructures as being peritectic in nature. The ∼RuAl phase was found to contain at least 27 at.% Pt (Alloy 4) and the ∼$PtAl_2$ phase exhibited up to 11 at.% solubility for ruthenium (Alloy 3). Although the ∼$RuAl_6$ phase was difficult to analyse accurately, since it was only found on a fine scale in Alloy 1 (Fig. 14), it showed solubility of at least 10 at.% platinum. Most of the other phases showed more limited solubilities for the ternary element: ∼$RuAl_2$, ∼Pt_2Al_3 and ∼PtAl contained only about 2 at.% of the third component, and ∼Ru_4Al_{13} had less than 1 at.% Pt.

Using the information from the solidification projection (Fig. 15) and the sequence of solidification from the microstructures, a liquidus surface was drawn to be consistent with the information derived from the samples and the binary phase diagrams (Fig. 16). From this, the ternary invariant reactions were derived (Table 2). The lowest temperature invariant reaction was peritectic, but the binary reactions from this has changed to eutectic at lower temperatures, giving the observed ∼Pt_5Al_{21} + (Al) and ∼$RuAl_6$ + (Al) eutectics (Alloy 13). Where insufficient experimental evidence was available to deduce a reaction, both alternatives are presented. The liquidus surface was dominated by the ∼RuAl phase, which stretches to within 10 at.% of the Al–Pt binary system, and ∼RuAl was involved in a number of subsequent reactions in the different alloys. The (Ru) phase also had a large liquidus surface. This is not surprising since both of these phases have very high melting points and they often dominate the phase diagrams in related systems [38]. Since Alloy 8 had no evidence of decomposed ∼Ru_2Al_3 and Alloy 3 did, it was more likely that this phase did form, but was fully decomposed in the subsequent peritectic reaction. The Al-rich corner was complex with very small surfaces, and alloys with very similar compositions solidified differently (for example, Alloys 1 and 13), and even within the same alloy, local differences in composition resulted in different solidification paths (again, Alloys 1 and 13).

Alloy 12 had Pt_5Al_3 as the second (matrix) phase, indicating that there is a maximum on the liquidus surface on the reaction line between (Ru) and ∼Pt_3Al liquid surfaces, allowing the ternary eutectic on the Pt-rich side.

Table 2
Invariant reactions for the Al–Pt–Ru system

Reaction
L → (Ru) + (Pt) + ∼Pt_3Al
L + (Ru) + ∼Pt_3Al → Pt_5Al_3
L + (Ru) → ∼RuAl + ∼Pt_5Al_3
L + ∼RuAl → β + ∼Pt_5Al_3
L + ∼PtAl + ∼RuAl → β
L + ∼RuAl → ∼PtAl + Pt_2Al_3
L + ∼RuAl → ∼Pt_2Al_3 + ∼$Ru_{18}Pt_{28}Al_{64}$[a]
L + Pt_2Al_3 → ∼RuAl + ∼$PtAl_2$
L + Pt_2Al_3 → ∼$PtAl_2$ + ∼$Ru_{18}Pt_{28}Al_{64}$[a]
L + ∼RuAl → ∼$Ru_{18}Pt_{28}Al_{64}$ + $PtAl_2$
L + Ru_2Al_3 → ∼RuAl + ∼$RuAl_2$
L + ∼RuAl + ∼$RuAl_2$ → ∼$Ru_{18}Pt_{28}Al_{64}$
L + ∼$Ru_{18}Pt_{28}Al_{64}$ + ∼$RuAl_2$ → ∼$Ru_{12}Pt_{15}Al_{73}$
L + ∼$Ru_{18}Pt_{28}Al_{64}$ → ∼$Ru_{12}Pt_{15}Al_{73}$ + ∼$PtAl_2$
L + ∼$RuAl_2$ → ∼$Ru_{12}Pt_{15}Al_{73}$ + ∼Ru_4Al_{13}
L + ∼$PtAl_2$ → ∼$Ru_{12}Pt_{15}Al_{73}$ + ∼Pt_8Al_{21}
L + ∼Pt_8Al_{21} → ∼$Ru_{12}Pt_{15}Al_{73}$ + ∼Pt_5Al_{21}
L + ∼$Ru_{12}Pt_{15}Al_{73}$ + ∼Pt_5Al_{21} → ∼$RuAl_6$
L + ∼$Ru_{12}Pt_{15}Al_{73}$ → ∼Ru_4Al_{13} + ∼$RuAl_6$[b]
L + ∼Pt_5Al_{21} → ∼$RuAl_6$ + (Al)
β → ∼PtAl + Pt_5Al_3
Ru_2Al_3 → ∼RuAl + ∼$RuAl_2$
∼$Ru_{18}Pt_{28}Al_{64}$ → ∼$Ru_{12}Pt_{15}Al_{73}$ + ∼$PtAl_2$

[a] Not enough experimental data available to conclude in which direction this reaction proceeds.

[b] Exit reaction subsequently changes to peritectic to be consistent with the Al–Ru binary.

6. Conclusions

Sixteen alloys were studied in the as-cast state using SEM with EDS and X-ray diffraction. A solidification projection and a liquidus surface were derived. The liquidus surface was dominated by the ∼RuAl phase which occurred to within 10 at.% of the Al–Pt binary. The (Ru) phase also had a large liquidus surface. ∼RuAl was found to contain at least 20 at.% platinum, ∼$PtAl_2$ exhibited up to 11 at.% solubility for ruthenium, ∼$RuAl_2$ exhibited up to 10 at.% solubility for platinum and ∼$RuAl_6$ showed solubility of at least 10 at.% platinum. Most of the other phases showed limited solubilities for the ternary element, less than 2 at.%: ∼Ru_4Al_{13}, ∼Pt_2Al_3, ∼Pt_5Al_3, ∼Pt_5Al_{21} and ∼PtAl. A ternary phase, ∼$Ru_{12}Pt_{15}Al_{73}$, was found near ∼Ru_4Al_{13}. Initial XRD analysis had already showed that the structure was primitive cubic, similar to ∼$RhAl_{2.63}$ and ∼$IrAl_{2.75}$, with a lattice parameter of 0.7712 ± 0.0005 nm. A high-temperature ternary phase, ∼$Ru_{18}Pt_{28}Al_{64}$, decomposes eutectoidally to form ∼$Ru_{12}Pt_{15}Al_{73}$ + ∼$PtAl_2$. The eutectoid decomposition of Ru_2Al_3 to ∼RuAl + ∼$RuAl_2$ was observed to be consistent with previous work. Four alloys had microstructural evidence of the β phase which decomposed eutectoidally to form ∼PtAl + ∼Pt_5Al_3.

Acknowledgements

This paper is published with the permission the CSIR-NML and Mintek. The financial support of the CSIR-NML, Mintek, the South African Department of Trade and Industry, Department of Science and Technology and the Platinum Development Initiative (AngloPlat, Lonmin and Impala) are gratefully acknowledged.

References

[1] L.A. Cornish, J. Hohls, P.J. Hill, S.N. Prins, R. Suss, D.N. Compton, 34th IOC on Mining and Metallurgy, Bor Lake, Yugoslavia, 2002, pp. 545–550.
[2] B. Tryon, T.M. Pollock, M.F.X. Gigliotti, K. Hemker, Scripta Mater. 50 (2004) 845–848.
[3] R. Huch, W. Klemm, Zeitschrift Anorganische Allgemeine Chemie 329 (1964) 123–135.
[4] G. Piatti, G. Pellegrini, J. Mater. Sci. 15 (1980) 2403–2408.
[5] P. Guex, P. Feschotte, J. Less Common Met. 46 (1976) 101–116.
[6] M.J. Schaller, Z. Metallkd. 70 (1979) 318–321.
[7] M. Ellner, U. Kattner, B. Predel, J. Less Common Met. 87 (1982) 305–325.
[8] L.E. Edshammar, Acta Crystallogr. 20 (1968) 2683–2688.
[9] T. Chattopadhyay, K. Schubert, J. Less-Common Met. 41 (1975) 19–32.
[10] S. Bhan, H. Kudielka, Zeitschrift Metallkunde 69 (1978) 333–336.
[11] A.J. McAlister, D.J. Kahan, Bull. Alloy Phase Diagrams 7 (1986) 47–51.
[12] Y. Oya, Y. Mishima, T. Suzuki, Zeitschrift Metallkunde 78 (1987) 485–490.
[13] A.S. Darling, G.L. Selman, R. Rushforth, Platinum Met. Rev. 14 (1970) 124–130.
[14] Y. Oya, Y. Mashima, T. Suzuki, International Conference of Martensitic Transformations, Japan, 1986, pp. 1009–1014.
[15] T. Biggs, P.J. Hill, L.A. Cornish, M.J. Witcomb, J. Phase Equilibria 22 (2001) 214–218.
[16] W. Obrowski, Naturwiss 47 (1960) 14.
[17] W. Obrowski, Metall (Berlin) 17 (1963) 108–112.
[18] S.M. Anlage, P. Nash, R. Ramachandran, R.B. Schwarz, J. Less Common Met. 136 (1988) 237–247.
[19] O. Schwomma, H. Nowotny, A. Wittmann, Monatshefte Chemie 94 (1963) 924–926.
[20] L.E. Edshammar, Acta Chem. Scand. 19 (1965) 2124–2130.
[21] L.E. Edshammar, Acta Chem. Scand. 20 (1966) 427–431.
[22] L.E. Edshammar, Acta Chem. Scand. 22 (1968) 2374–2375.
[23] W.G. Jung, O.J. Kleppa, Metall. Trans. B 23B (1992) 53–56.
[24] T.D. Boniface, L.A. Cornish, J. Alloys Compd. 234 (1996) 275–279.
[25] T.D. Boniface, L.A. Cornish, J. Alloys Compd. 233 (1996) 241–245.
[26] W.G. Jung, O.J. Kleppa, Metall. Trans. B: Process Metall., 23B (1992) 53–56.
[27] S. Mi, S. Balanetskyy, B. Grushko, Intermetallics 11 (2003) 643–649.
[28] I.M. Wolff, Metall. Trans. A, 27A (1996) 3688–3699.
[29] N. Ilić, R. Rein, M. Goken, M. Kempf, F. Soldera, F. Mucklich, Mater. Sci. Eng. A 329–331 (2002) 38–44.
[30] F. Mücklich, N. Ilić, Intermetallics 13 (2005) 5–21.
[31] T.B. Massalski, in: T.B. Massalski (Ed.), Binary Alloy Phase Diagrams, vol. 1, ASM International, 1990.
[32] T. Biggs, Ph.D. Thesis, University of the Witwatersrand, 2001.
[33] ICDD, International Centre for Diffraction Data (ICDD), Powder Diffraction File, International Centre for Diffraction Data, Pennsylvania, USA, 2001.
[34] ICSD, Inorganic Crystal Structure Database (ICSD), FIZ Karlsruhe, Eggenstein-Leopoldshafen, Germany, 2002.
[35] Crystallographica, Crystallographica Oxford Cryosystems Ltd., 2000.
[36] F.A. Rajabalee, Wincell 1.1: A Windows Package of DOS Routines for Unit Cell Refinements, in: F.A. Rajabalee (Ed.), Bordeaux, France, 2000.
[37] S.N. Prins, P.S. Boucher, L.A. Cornish, 21st European Crystallographic Meeting (ECM-21), Durban, August 24–29, 2003, p. 246.
[38] L.A. Cornish, M.J. Witcomb, P.J. Hill, I.J. Horner, South Afr. J. Sci. 95 (1999) 517–525.